

CONSTRAINING THE PHYSICAL CONDITIONS IN THE JETS OF γ -RAY FLARING BLAZARS USING CENTIMETER-BAND POLARIMETRY AND RADIATIVE TRANSFER SIMULATIONS. II. EXPLORING PARAMETER SPACE AND IMPLICATIONS

PHILIP A. HUGHES, MARGO F. ALLER, AND HUGH D. ALLER
 Astronomy Department, University of Michigan, Ann Arbor, MI 48109-1107
Draft version December 9, 2014

ABSTRACT

We analyze the shock-in-jet models for the γ -ray flaring blazars 0420-014, OJ 287, and 1156+295 presented in Aller et al. (2014, Paper I), quantifying how well the modeling constrains internal properties of the flow (low energy spectral cutoff, partition between random and ordered magnetic field), the flow dynamics (quiescent flow speed and orientation), and the number and strength of the shocks responsible for radio-band flaring. We conclude that well-sampled, multifrequency polarized flux light curves are crucial for defining source properties. We argue for few, if any, low energy particles in these flows, suggesting no entrainment and efficient energization of jet material, and for approximate energy equipartition between the random and ordered magnetic field components, suggesting that ordered field is built by non-trivial dynamo action from the random component, or that the latter arises from a jet instability that preserves the larger-scale, ordered flow. We present evidence that the difference between orphan radio-band (no γ -ray counterpart) and non-orphan flares is due to more complex shock interactions in the latter case.

Subject headings: galaxies: jets — magnetic fields — polarization — radiation mechanisms: nonthermal — shock waves — AGN: individual(0420-014,OJ 287,1156+295)

1. INTRODUCTION

For most of the history of broadband studies of active galactic nuclei (AGN) it has been the paradigm that the higher the energy of the emission, the closer to the central engine that emission arises, with the highest energies coming from the immediate environment of the supermassive black hole and accretion disk (Marscher 2006). While this is likely to be true of the quiescent emission, it has become clear over the last few years that *flare* emission at high energies is *not* situated close the central engine, but is, at least approximately, cospatial with the region within which VLBI imaging reveals stationary or propagating knots in the radio waveband. Evidence for an association between high energy (specifically GeV) and radio flaring is summarized in Aller et al. (2014, hereafter Paper I), and rests primarily on the observation that γ -ray flaring always occurs at or near to the rise portion of a radio-band event (first noted by Valtaoja & Teräsranta 1995, 1996), and component ejections seen in 43 GHz VLBI monitoring data are temporally associated at a statistically significant level with γ -ray flares (e.g., Jorstad et al. 2001). The EGRET results have been confirmed by recent studies using the wealth of data from Fermi. For example, Agudo et al. (2011) have presented strong evidence that γ -ray flaring in OJ 287 is located > 14 pc from the central engine, Jorstad et al. (2013) present evidence that γ -ray and low-frequency events are cospatial in the source 3C 454.3, while Ackermann et al. (2014) tentatively associate a knot seen in 43 GHz imaging of PKS 1222+216 with a γ -ray flare, also putting the event in the parsec-scale flow. However, statistical studies based on cross correlations of γ -ray and radio-band light curves have been less clear-cut in providing evidence that the same

disturbance is responsible for activity in both bands: Max-Moerbeck et al. (2014) find that only one out of 41 sources (using 4 yr of 15 GHz observations from the Owens Valley Radio Observatory 40-m monitoring program) show correlated γ -ray-radio-band activity at a significance greater than 3σ (and only 4 sources have any statistically significant correlation); it is likely that the correlation analysis is limited by uneven sampling, and the almost continuous activity exhibited by most sources. More promisingly, Kovalev et al. (2009) find that radio jets are more active within months of Fermi-detected γ -ray emission. While the statistical studies are inconclusive, the association of γ -ray and radio-band events, on a case-by-case basis, supports the view that the γ -ray mission arises at parsec-scales, and motivation for the modeling discussed here.

On the premise of a strong connection between the radio-band and γ -ray flares, detailed modeling of the former provides a powerful tool with which to help understand the origin of the high energy emission, and thus the flow dynamics and particle kinematics of relativistic flows. A wealth of data – multifrequency light curves in total and polarized flux from single dish observations, and component fluxes, ejection times, and speeds from VLBI observations – coupled with radiation transfer calculations for shocks propagating in a diverging flow – the widely accepted picture for the interpretation of radio-band data – can provide a detailed picture of the flow structure, dynamics, state and orientation. That provides a framework within which to understand the physical origin of the γ -ray flares, and can potentially shed light on why some radio flares have no high energy counterpart, and vice versa.

Motivated by these considerations, we extended our original shock modeling (Hughes et al. 1985; Hughes, Aller & Aller 1989a,b) to include arbitrary

shock obliquity with respect to the flow direction (Hughes, Aller & Aller 2011), and used that study as the basis of models for three sources which displayed cotemporal radio-band and γ -ray flares, and which had sufficiently well-defined structure in their total and polarized light curves that model-fitting to the several sub-flares that comprise each distinct outburst was viable (Paper I). The selected sources were the QSO 0420-014, the BL Lac object OJ 287, and the FSRQ 1156+295. We found that the general structure and spectrum of both the total and polarized flux light curves could be reproduced with forward moving shocks, preferentially oriented transversely to the flow direction, with OJ 287 being distinct in needing a significantly oblique shock structure, and very low cutoff energy for the radiating particle distribution.

The modeling was able to provide an estimate of the angle at which the observer views the flow: that parameter is very well-constrained because of the sensitivity of the level of polarized flux to the direction from which the source is viewed. The source parameters, including the viewing angle, are determined independently of VLBI observations, and yet provide component speeds and viewing angle in agreement with those found from VLBI data for the sources modeled, validating the modeling. A particular value of the modeling is that it enables an estimation of these (and other) source properties, for sources for which no VLBI data exist.

It was noted in Paper I that one of the best-determined source parameters is the observer's angle of view with respect to the jet axis, as this plays a major role in establishing the level of polarized emission, and small changes in the viewing angle have a large impact on the amplitude of P . The scope of Paper I did not allow a full discussion of the complete set of model parameters, nor an exploration of the impact of changing those parameters on the model light curves, and thus a quantitative assessment of how well-constrained each parameter is. It is the purpose of the current paper to discuss the choice of parameter values, quantify how well each is determined, and illustrate the changes to the model light curves that result from variation in those parameters to which the modeling is most sensitive. Section 2 provides a broad overview of all parameters needed to specify a source model, while Section 3 contains a detailed analysis of the roles played by the low-energy cutoff in the radiating particle spectrum, the axial magnetic field strength, the flow Lorentz factor, the observer's angle of view with respect to the jet axis, and the azimuthal angle of view. The azimuthal angle is not significant for transverse shocks, but it is potentially important if the shock is highly oblique. Section 4 explores how changing the number and strength of shocks contributing to a single radio outburst impacts the light curve in the context of the 'orphan flare' in the light curve of 1156+295. It was noted in Paper I that the modeling ignores retarded time effects, since they produce negligible changes in the light curves; justification for that is presented in an appendix.

2. MODEL PARAMETERS

All computations have been performed in a volume of $61 \times 61 \times 600$ cells. The lateral extent of the volume is sufficient to allow the modeling of a diverging flow, while the length can accommodate multiple shocks within the

flow at one time. The additional computational resources needed to explore a larger volume would limit the range of sources, events, and parameters explored, and is unnecessary judged by the absence of artifacts associated with limited resolution in the light curves.

Each simulation has used a jet with opening half-angle 2.4° , with initial radius 1/12th the lateral extent of the computational volume. These were chosen to optimize the use of the volume: adiabatic expansion of a component reduces the total and polarized flux to close to the jet quiescent level by the time that component has traversed the volume. Models are insensitive to the opening angle to the extent that an increase (decrease) in the angle causes a more (less) rapid fall of flux as the component propagates; this translates into a smaller (larger) number of computational time steps being mapped into the observed event duration during modeling, thus using the volume less effectively, but not changing the general trends with time and frequency seen in the model light curves. Changing the flow opening angle will change the distribution of flow velocity vectors seen by an observer placed at some viewing angle from the flow axis, but for quite well-collimated flows, the impact of this on the light curves will be subtle, and matching models to data provides little constraint on the opening angle.

Computations are performed in dimensionless units, with particle density, magnetic field strength, line-of-sight source extent and observational frequency scaled with fiducial values. Associating a particular model event with data then establishes a length (through association with structure on a VLBI map) or a time (through association with a light curve flare duration). With absolute time (length) established, the speed of light then establishes an absolute length (time). However, that still leaves particle and energy densities unknown, and thus a model is scaled to match the peak model flux at the highest frequency to the peak flux of the modeled flare. For the same reason, opacity (a function of line-of-sight source extent, particle and field densities, and observational frequency) is unknown, and is incorporated using the same scaled quantities, subject to an overall arbitrary scaling. Effectively, a target optical depth for a representative line-of-sight, and fiducial values of all pertinent physical quantities, are set, and the local opacity is scaled throughout the volume accordingly. In modeling, this parameter is adjusted to give the best match to the spectral behavior of the event at peak flux.

The radiating particle energy distribution is assumed to follow a power-law in Lorentz factor, $n(\gamma)d\gamma = n_o\gamma^{-\delta}d\gamma$, $\gamma > \gamma_i$. As noted below, previous studies suggest a fairly flat spectrum, and thus that there must be an upper cutoff to keep the total energy in the particle distribution finite. However, that cutoff is assumed to be well above the energies seen by GHz-band University of Michigan Radio Observatory (UMRAO) data, and is not pertinent to the GHz-band modeling. We plausibly, but arbitrarily, assume that the particles seen through their synchrotron emission in the central UMRAO band (8 GHz) have a fiducial Lorentz factor $\gamma_c = 10^3$. This implies a magnetic field strength in the emitting region through $\gamma_c^2 \sim \nu(8\text{ GHz})/\nu_G$, where ν_G is the particle gyrofrequency. A different choice of γ_c would imply a different field strength, and concomitant change in flux

density. However, as we are concerned only with the spectral and temporal form of the light curves, which are subject to an arbitrary scaling, this has no impact on the modeling. The purpose of setting γ_c is to establish the extent to which a certain choice of γ_i extends the spectrum to include particles that can contribute significantly to internal Faraday effects. Such an approach assumes that no Faraday effects arise from a distribution of (cold) thermal electrons within the jet, which is consistent with the most recent studies, such as the analysis of circular polarization in the source PKS B2126-158 by O’Sullivan et al. (2013), who also summarize arguments against there being a significant thermal electron content in such flows. Additionally, Hovatta et al. (2012) present a discussion of MOJAVE observations showing that they are consistent with external Faraday screens being responsible for the polarization behavior exhibited by *most* sources.

The power-law index of the radiating particle distribution is determined by fixing the optically-thin frequency spectral index as $\alpha = 0.25$, where α is defined by $S(\nu) d\nu = S_0 \nu^{-\alpha} d\nu$. This value is chosen by inspection of the data for many UMRAO-observed sources, which typically display a rather flat spectrum even in the optically-thin state. Since the work of Blandford & Königl (1979) it has been conventional wisdom that the flat optically-thin spectra of blazars are a consequence of summing the multiple segments that make up a quiescent flow, each with slightly different peak frequency. However, the first detailed shock models (Hughes, Aller & Aller 1989b) suggested that a flat spectrum is an intrinsic feature of these flows, a truncation of the jet being needed for a good fit of the model to the data. This is not surprising: as discussed by Marscher (2006), self-similarity cannot extend down to the region of jet formation. An observable jet starts some distance from the central engine, possibly where particle acceleration and field amplification occur at a recollimation shock (Cawthorne et al. 2013).

As discussed in Hughes, Aller & Aller (2011), three components of magnetic field have been considered, two (random, and ordered helical) widely believed to play a role in determining the character of the emitted radiation, and a third (ordered axial) to provide a well-defined electric vector position angle (EVPA) in the quiescent state. Of the two potentially dominant components, a random field is established in each jet as set out in Hughes, Aller & Aller (2011), while the helical component discussed in that paper has not been incorporated in the current modeling, as the previous study showed that a significant contribution (when the helical component contributes of order half, or more, of the total magnetic energy density) from such a field predicted evolution of the EVPA not in agreement with UMRAO data. Modeling of the sources 0420-014, OJ 287, and 1156+295 as discussed in Paper I led to the unexpected result that the axial magnetic field, originally thought to be unimportant during outbursts, and set to provide a well-defined quiescent EVPA, can play a significant role in determining the properties of the polarized emission while a source is in outburst. The magnitude of that is thus an important parameter, and is characterized by B_z , in units such that the average random field has unit magnitude: $\langle B_{\text{ran}}^2 \rangle = 1$. Thus a flow with *only* the axial field would

have a magnetic energy density a fraction \bar{B}_z^2 that of the purely random case.

The Lorentz factor of the bulk, unshocked flow (γ_f), is specified independently of the shock strengths, and is typically in the range 5-10. The compression of each shock is specified as a fraction $\kappa < 1$, so that the passage of a shock compresses unit length to length κ . For a relativistic equation of state and given shock obliquity this compression uniquely determines the upstream and downstream Lorentz factors in the frame of the shock transition (Hughes, Aller & Aller 2011). The speed of the shock transition can then be calculated given the bulk Lorentz factor, once a choice between reverse or forward shocks has been made. A shock system is thus completely specified by choice of bulk Lorentz factor, shock obliquity, shock sense (forward or reverse), and the compressions of the individual shocks. Additionally, each shock has a certain start time and has a length (extent of the shocked region) expressed as a fraction of the quiescent flow length.

The remaining fundamental parameters are the polar (θ) and azimuthal (ϕ) angle of the observer. The jet axis provides a natural reference for the polar angle ($\theta = 0$), while the zero-point of the azimuthal angle is arbitrary. For a transverse shock (i.e., with the shock normal parallel to the jet axis) the azimuthal orientation of the observer will play no role in what is seen. However, as a general rule, ‘transverse shocks’ are modeled with a slight offset (typically 1°), in part as it is computationally convenient to avoid infinities in the analytic forms used to compute speeds and deflections, but also because running a model through a range of azimuthal angles can then give insight into the sensitivity of the model to slight variations in obliquity.

Formally, an additional parameter, the orientation of the shock normal with respect to an arbitrary azimuthal reference direction, ψ , can also be specified. However, that is degenerate with the observer’s azimuthal viewing angle, ϕ , and need not be considered separately. As noted in Hughes, Aller & Aller (2011) and Paper I, the azimuthal angle does not play a major role in determining the *general form* of the total and polarized flux light curves, but, in particular for very oblique shocks, the appropriate choice of angle can be important for reproducing certain details of the data – such as the relative percentage polarization of shocks within a flare envelope.

In summary, the fundamental parameters for exploration are those characterizing the internal state of the quiescent flow, the bulk dynamics and orientation of that flow, and the attributes of the disturbances (shocks) to that flow, giving rise to non-steady emission; namely

- the low-energy cutoff of the radiating particle distribution, γ_i , and the axial magnetic field characterized by B_z ;
- the bulk Lorentz factor (γ_f) and viewing angle (θ , ϕ) of the flow;
- the obliquity (η), sense (**F** or **R**), compression (κ), start time, and length of each shock.

3. PARAMETER EXPLORATION

The obliquity (η), sense (**F** or **R**), compression (κ), start time, and length of each shock are adjusted as

part of the modeling process. This parameter set, in part, defines a distinct source model. The obliquity, sense, compression and length of each segment of shocked flow will depend on the (unspecified) process that originally set up the shocks, while the start times establish a causal relationship between these events and both evolving VLBI structures and flaring in other emission bands. Values of these parameters for the models of sources 0420-014, OJ 287, and 1156+295 are presented and discussed in Paper I. They are typical of values found in earlier shock models of blazar flares (Hughes, Aller & Aller 1989b; Hughes et al. 1991), except that the recent modeling favors forward moving, rather than reverse, shocks.

On the other hand, the low-energy cutoff of the radiating particle distribution, γ_i , the axial magnetic field, B_z , the bulk Lorentz factor (γ_f), and the viewing angle (θ , ϕ) of the flow, are fundamental parameters of the jet/shock system. There are implications for jet magnetohydrodynamics and particle acceleration processes in the case of the cutoff, field and Lorentz factor, and implications for the appearance of flares – and potentially the relative prominence of flares in different parts of the radio spectrum – in the case of all these parameters. It is thus important to understand how well these quantities are established by the modeling. In particular, exploring how models change as these parameters are varied will establish how different these fundamental parameters are in sources with behavior broadly similar to that of the modeled sources, but with differences in detail – for example, in the total flux density spectrum, or in the amplitude and complex variations of the polarized flux.

We consider each of these parameters below, using the models of 0420-014 and 1156+295 (with transverse shocks) and OJ 287 (with oblique shocks) as discussed in Paper I. A ‘library’ of light curves (S , P and EVPA at each of three frequencies) could be constructed for a single flare over a grid of these parameters, and a sequence of shock obliquities, but a well-sampled exploration of a 6-parameter space would lead to an unmanageable set of complex plots, which would in fact provide little physical insight, because a) most interest lies in the complex interaction of multiple events – indeed, the UMRAO data show that single shock models are physically unrealistic; and b) the variation of a given parameter is often significant in a particular way: for example, variation of the contribution of an on-axis magnetic field significantly influences the degree and structure exhibited by the percentage polarization, leaving the total flux density largely unchanged. It is therefore more useful to focus on the consequences of varying one parameter at a time, in the context of a representative model.

The resulting figures are complex (multiple panels, each containing multiple curves – one for each of the harmonically related frequencies modeled). Overlaying a number of such displays leads to graphs of such density and complexity as to be unreadable, while a mosaic of plots renders each too small for the detail to be seen, and does nothing to facilitate appreciating the changes that occur as a parameter is varied. To show the range of behavior we display two sets of model curves only – for each extreme of the parameter range – to highlight the consequence of parameter variation, and animations are available in the online version of the journal that enable to reader to step through, pause, and replay sequences

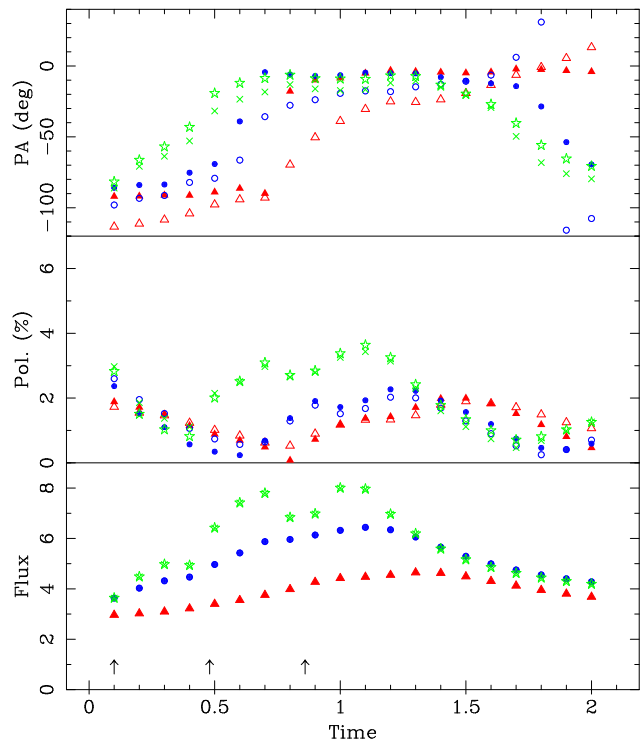


Figure 1. The model for 0420-014 at two extremes of the low-energy spectral cutoff: $\gamma_i = 25$ is shown using unfilled triangles, circles and crosses for the frequencies corresponding to the UMRAO frequencies of 4.8, 8.0, and 14.5 GHz (the same convention adopted in Paper I), while $\gamma_i = 75$ uses filled triangles, circles, and solid crosses. Note that the flux curves do not change, and only one set of points is evident in the bottom panel. The onset time of each shock is shown by arrows in the bottom panel. An mpeg animation showing in detail the variation of the light curves with change in model parameter is available online.

of models.

3.1. Low Energy Cutoff

In the absence of a ‘cold’ plasma component, Faraday effects are associated with the relativistic particles in the low energy part of the radiating particle spectrum. Following the notation of Jones & O’Dell (1977), whose analysis has formed the basis of our modeling since the work of Hughes, Aller & Aller (1989b), such effects depend on the normalized rotativity

$$\zeta_v^* = \zeta_{v\alpha}^* \frac{\ln \gamma_i}{\gamma_i} \left(\frac{\gamma_c}{\gamma_i} \right)^{2\alpha+1} \left(\frac{\nu}{\nu_c} \right)^{\alpha+1/2} \cot \vartheta, \quad (1)$$

where $\zeta_{v\alpha}^*$ is a constant of order unity, and ν_c is the emission frequency for particles of energy γ_c . For observations at frequency $\nu \sim \nu_c$, a random field element oriented with respect to the observer such that $\cot \vartheta \sim 1$, and, as noted above $\alpha = 0.25$, for the rotativity to play a significant role we need

$$\frac{\ln \gamma_i}{\gamma_i} \left(\frac{\gamma_c}{\gamma_i} \right)^{1.5} \gtrsim 1, \quad (2)$$

or $\gamma_i \lesssim \gamma_c^{0.6}$. Given $\gamma_c = 10^3$, this implies we can expect to see significant Faraday effects for γ_i less than about 60.

The parameter sequence shown in Figure 1 (animation online) spans the range $25 \leq \gamma_i \leq 75$, and is based on

the model for 0420-014, for which a value of $\gamma_i = 50$ was adopted.¹ The three panels are, from bottom to top, the total flux density, the percentage polarization, and the EVPA (position angle of the electric vector of the polarized emission) at three harmonically related frequencies. In this and the following cases (with one exception noted below) the figures show the models from the first and last frames of the animation sequences, with the model for the lowest value of the varied parameter depicted using unfilled triangles, circles and crosses for the frequencies corresponding to the UMRAO frequencies of 4.8, 8.0, and 14.5 GHz (the same convention adopted in Paper I), while the model for the highest value of the parameter is shown with filled triangles, circles, and solid crosses. Arrows in the bottom panel show the onset time of each shock.

Changes in the percentage polarization are small; indeed, they are perceptible only for $\gamma_i < 50$. Below this value, lower values of γ_i lead to a slightly raised value of the percentage polarization (tenths of a percent) at the lowest frequency (4.8 GHz) between the peaks of the second and third shocks. The increased Faraday depth (significant only at the lowest frequency) causes a slight rotation of the EVPA of the emission from the most optically thick part of the source, changing the percentage polarization integrated over the entire jet. However, this effect is too small to play any role when confronting the data with models designed only to reproduce general trends.

For the highest value of γ_i explored here, there is a small separation in the EVPAs with frequency at the initial time, which exhibits no significant change between values of 65 and 75, indicating that the small residual difference is opacity-related. The separation of the EVPA curves with frequency increases during the onset of the outburst because of the opacity-induced delay in seeing the orthogonally-polarized shock emission. Quantitatively, this trend is not significantly influenced by the value of γ_i . Towards the end of activity, emission at the highest frequency has become sufficiently optically-thin that the quiescent flow begins to dominate again, and there is reversion towards the original EVPA. Only very low cutoff values, and opacity higher than that adopted in this model, can be expected to reveal the effects of the cutoff in the flare light curves, as for example in the case of OJ 287 (Paper I).

The sense of Faraday rotation is dependent on the sense of the magnetic field component along the line-of-sight, and while a finite number of randomly-oriented magnetic cells will lead to a dispersion in net rotation over a set of realizations of that field, the effects we have discussed above are associated with the ordered, axial field of the flow. In that sense, the absence of an ordered field is degenerate with a higher value of the cutoff energy.

3.2. Axial Magnetic Field

We now discuss how sensitive the model fitting is to an ordered component of the magnetic field. The parameter sequence shown in Figure 2 (animation online) spans the range $0.05 \leq \bar{B}_z \leq 1.0$, and is based on the

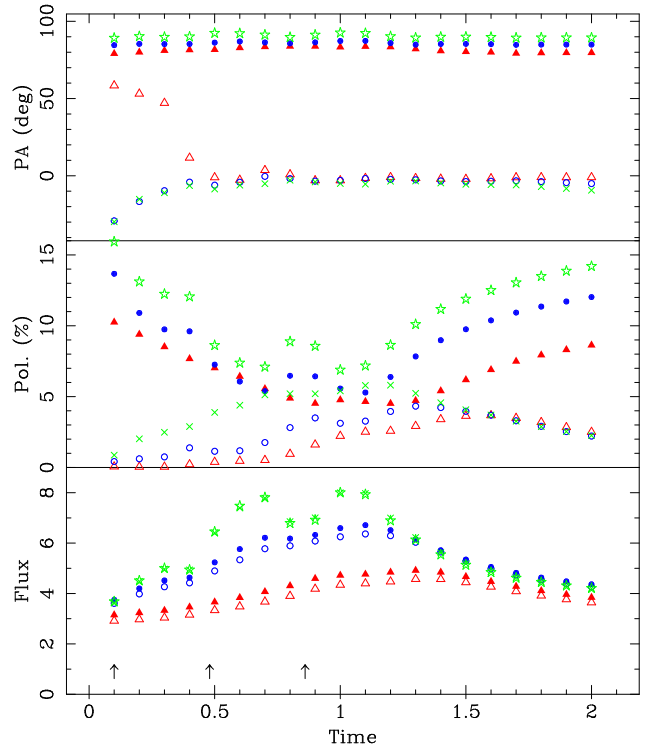


Figure 2. The model for 0420-014 at two extremes of the mean field contribution: $\bar{B}_z = 0.05$ and 1.0 . The symbols are as for Figure 1. An mpeg animation showing in detail the variation of the light curves with change in model parameter is available online.

model for 0420-014, for which a value of $\bar{B}_z = 0.4$ was adopted. (Note that in the animation the sample values are not uniformly distributed in the adopted range.) The ‘fiducial’ value corresponds to a magnetic energy density $\bar{B}_z^2 \sim 0.16$, so that the mean field contributes less than 20% of the energy density contributed by the random component. Inspection of the parameter sequence reveals that a change in the character of the polarized emission – the percentage polarization and EVPA, and their frequency and time dependence – occurs at $\bar{B}_z \sim 0.5$, at which point the mean field is contributing $\sim 20\%$ of the total magnetic energy density.

The quite rapid switch to a high degree of polarization, and EVPA orthogonal to that displayed during the shock-dominated, weak mean field case, for values $\bar{B}_z \gtrsim 0.5$ is not surprising. As noted by Hughes, Aller & Aller (2011), even small spurious Fourier components associated with generating a random magnetic field by selecting random phases and amplitudes for the Fourier transform of the magnetic vector potential can lead to significant spurious polarized flux. However, this does lead to the question of how plausible it is to invoke an ordered magnetic field to explain the amplitude and detailed structure of blazar polarized flux light curves, if a modest increase in the strength of that component can lead to features (very high percentage polarization, for example) never seen in those same light curves.

In fact, the fundamental premise of our modeling – that these flows are turbulent – suggests that the ordered field is not a direct manifestation of the central black hole/accretion disk system to which the jet is tied, but is generated *in situ* through a dynamo process (Eilek & Hughes 1991). Mean field dy-

¹ Animations of model sequences are available at: <http://dept.astro.lsa.umich.edu/~phughes/GALLERY/APJ14/>.

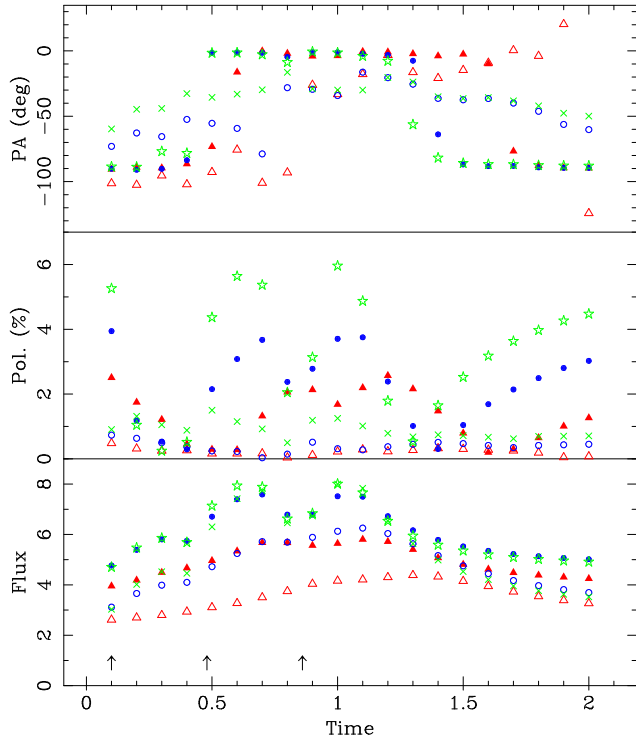


Figure 3. The model for 0420-014 at two extremes of the flow Lorentz factor: $\gamma_f = 2.0$ and 43.0. The symbols are as for Figure 1. An mpeg animation showing in detail the variation of the light curves with change in model parameter is available online.

namous in sheared, turbulent flows are known to occur (Rogachevskii & Kleeorin 2003), and while the process has not been explored for a cylindrical geometry (for which it can be speculated that the mean field takes the form of a force-free flux tube), shearing box simulations (Yousef et al. 2008) show the dominant mean field to be in the sense of the flow – which is along the axis in the case of a jet. It would then be expected that a mean field would grow, and then saturate at an energy density some fraction of order unity that of the kinetic energy density of the underlying turbulence; the latter would be expected to be comparable to the energy density in the random field. This is impossible to quantify, as there are inconsistencies between state of the art analytic theory and simulations in this field, and it remains impossible to apply the latter to realistic values of scale separation, Reynolds number, etc. (e.g., Park et al. 2013). However, simulations such as presented in that study strongly suggest such a saturation, as do recent studies of relativistic turbulence (Zrake 2014). In the context of this interpretation, the importance of a weak ordered field in explaining the light curves, while never dominating the light curves, is evidence supportive of the scenario in which any large scale field grows through dynamo action in a fundamentally turbulent flow.

3.3. Bulk Lorentz Factor

The parameter sequence shown in Figure 3 (animation online) spans the range $2.0 \leq \gamma_f \leq 43.0$, and is based on the model for 0420-014, for which a value of $\gamma_f = 5.0$ was adopted, and for which the viewing angle is 4° . Each set of plots in the sequence increases the Lorentz factor by 1.05 relative to the speed of the previous case. For fixed angle of view and observing frequency, a change

in the Lorentz factor leads to a change in the Doppler factor, and thus to a change in the emission frame frequency. The adopted value of the opacity was therefore adjusted to compensate for this, so that the asymptotic spectral shape (the spectral slope at the end of the flare, when close to quiescent) was the same in each case. The opacity drops by a factor ~ 2 per step in Lorentz factor through the first half of the sequence, and then asymptotes to a value ~ 0.024 times the initial value, between Lorentz factor values of 12.2 and 16.7; beyond this point in the sequence, the viewing angle lies outside the critical ($1/\gamma$) cone of the flow.

The spectral shape during flaring changes along this sequence because the Lorentz factor of the shocked flow differs from that of the quiescent flow, the spectral characteristics of which are used to normalize the opacity. (The quiescent flux rises along the sequence because the peak flux is normalized to that of the modeled data, and the spectrum becomes shallower.) For the model of 0420-014 the Lorentz factor of the shocked flow is ~ 8 , required to yield the necessary shock compression, in the forward shock case. In the sequence under discussion, the Lorentz factor is varied, but the shock compressions adopted for the 0420-014 model are retained from case to case. For flows slower (faster) than the fiducial case, a given compression is achieved with a shocked flow with Lorentz factor < 8 (> 8). The adjustment to the opacity thus under-compensates during the flare for the slower flows. As for the quiescent spectral shape, that of the flare asymptotes at high flow speed.

For the smallest Lorentz factor of the sequence the percentage polarization is very low – rising just above 1% at the highest frequency, and negligible at the lower frequencies. It rises rapidly along the sequence, attaining values in the range 2-4% for the Lorentz factor of the 0420-014 model, peaks with maximum value $\sim 6\%$ at the highest frequency for $\gamma_f \sim 12$ and then declines slowly. As noted above, this corresponds to the critical cone of the flow passing through the observer’s line-of-sight; at that angle the observer sees radiation emitted orthogonal to the flow direction, which for a compression transverse to the flow will maximize the polarization. That orientation also maximizes the projection of the mean axial field on the observer’s plane-of-sky. Below $\gamma_f \sim 12$ the rapid change in degree of polarization with Lorentz factor provides a strong discriminant between models for data such as those for 0420-014, while higher values of the Lorentz factor are excluded in this case by both the high model percentage polarization in the flare-state, and in quiescence, where the polarized emission is significantly influenced by the axial mean field (seen in the emission frame at an angle of 37° for $\gamma_f = 43$).

For the lowest Lorentz factors the degree of polarization is low, the EVPA is subject to substantial spread with frequency, and trends are difficult to define. By $\gamma_f \sim 3.5$ the polarization has risen to a level that allows a well-defined EVPA, the trends in which then persist across the sequence to the highest Lorentz factor explored. The 4.8 GHz data are sparse, but the 8.0 and 14.5 GHz data points and the model exhibit a swing in EVPA by $\sim 90^\circ$ that are in agreement.

3.4. Polar Viewing Angle

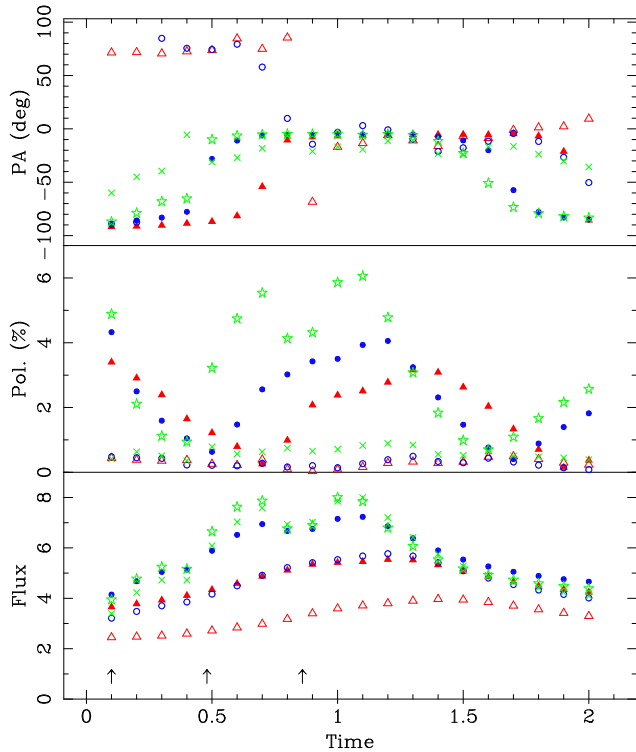


Figure 4. The model for 0420-014 at two extremes of the polar viewing angle: $\theta = 1.6$ and 5.6° . The symbols are as for Figure 1. An mpeg animation showing in detail the variation of the light curves with change in model parameter is available online.

The parameter sequence shown in Figure 4 (animation online) spans the range $1.6 \leq \theta \leq 5.6^\circ$, and is based on the model for 0420-014, for which a value of 4.0° was adopted for the polar viewing angle. There is a non-negligible change in the character of the total flux as the viewing angle changes, but this is almost entirely associated with the fact that the Doppler factor, and thus Doppler shift, change with viewing angle. As the angle of view increases, for fixed frequency of observation, the Doppler factor diminishes leading to a higher emission frame frequency, a less optically thick flow, and a flatter spectrum. As noted above, when exploring a range of flow Lorentz factors the opacity was adjusted to compensate for this effect. This was essential, as without it the almost two orders of magnitude change in opacity, a completely optically thick flow would have appeared over most of the parameter range explored. Here the small range in Doppler factors means that it is not essential to compensate for its change, allowing a direct exploration of changes in polar viewing angle.

As noted above, the Lorentz factor of the shocked flow in the 0420-014 model is ~ 8 , for which the critical angle is $\sim 7^\circ$. The range of viewing angles thus spans the inner part of the critical cone, the degree of polarization rising rapidly – to $\sim 6\%$ at the highest frequency – as the viewing angle approaches the critical value at which the percentage polarization is a maximum for a compression transverse to the flow. Note that the flow does not become appreciably optically-thin at any angle, so the change in degree of polarization is largely a geometric effect.

The two primary shocks in the 0420-014 model have almost identical compressions of $\kappa = 0.65$, for which

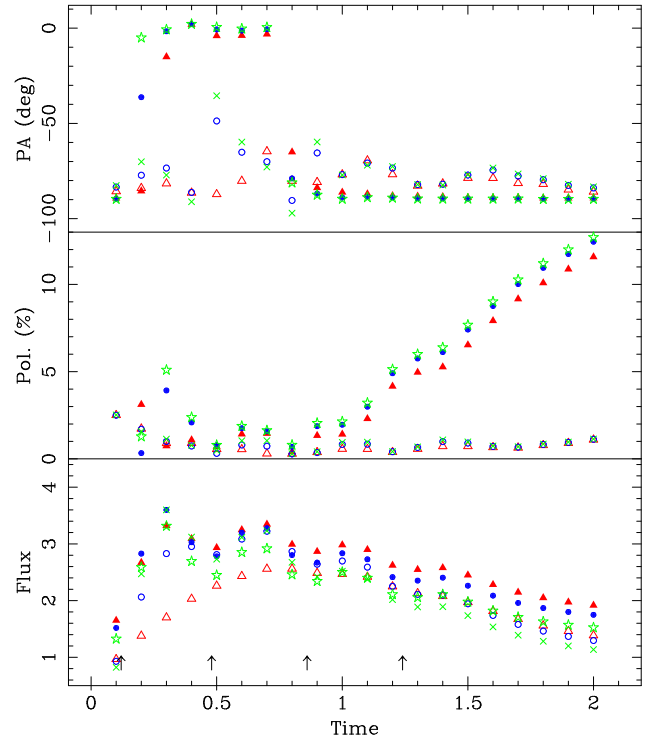


Figure 5. The model for 1156+295 at two extremes of the polar viewing angle: $\theta = 0.5$ and 3.5° . The symbols are as for Figure 1. An mpeg animation showing in detail the variation of the light curves with change in model parameter is available online.

the maximum polarization is $\sim 26\%$ (Hughes et al. 1985) in the simple case of an optically-thin, compressed flow (and for the maximum polar angle explored, and given shocked flow speed, is only marginally less, $\sim 24\%$). In this case, and for almost all UMRAO sources, that the observed percentage polarizations are substantially less, rarely above 10% (Aller et al. 2003), is attributable to a combination of opacity and cancellation from a modest, but non-negligible axial field component. Certainly, picking a data point at random from a source at random will almost invariably yield a single digit percentage polarization, and it might be thought that models cannot expect to do better than predict such single digit percent polarization. However, at least as long as one looks over a restricted enough time interval, for example a time spanning a few flares, sources have a typical and distinct range of this characteristic. For example, the periods containing the modeled flares in 0420-014, OJ 287 and 1156+295 (Paper I) display values between 1 and 4%, 0 and 9%, and 1 and 5%, respectively. Thus as a rule, and not just for our modeled sources, there is distinctive behavior that models can aspire to match quantitatively. As seen in the parameter sequence, the model percentage polarization is very sensitive to viewing angle, so this is a particularly well-constrained parameter of the model.

For comparison, the parameter sequence shown in Figure 5 (animation online) spans the range $0.5 \leq \theta \leq 3.5^\circ$, and is based on the model for 1156+295 for which a value of 2.0° was adopted, and which has a more substantial axial magnetic field: $\bar{B}_z = 0.7$. The quiescent flow has Lorentz factor $\gamma_f = 10.0$, for which the critical angle is 5.7° , so the parameter sequence probes angles within the critical cone of that flow. At late times emission from

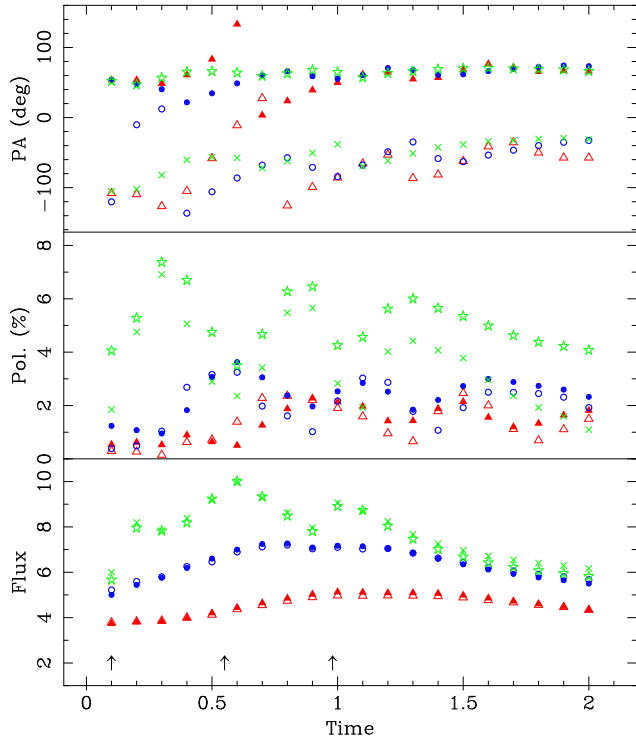


Figure 6. The model for OJ 287 at two extremes of the polar viewing angle: $\theta = 0.5$ and 2.5° . The symbols are as for Figure 1. An mpeg animation showing in detail the variation of the light curves with change in model parameter is available online.

the quiescent flow begins to dominate, and the percentage polarization rises above 10% for the larger angles in the sequence because of the strong axial field, seen during quiescence at $\sim 40^\circ$ to the plane of the sky in the emission frame. We attribute the fact that UMRAO data rarely display such high levels of polarized emission to the fact that, as noted in Hughes, Aller & Aller (2011), truly quiescent states are themselves a rarity.

The parameter sequence shown in Figure 6 (animation online) spans the range $0.5 \leq \theta \leq 2.5^\circ$, and is based on the model for OJ 287 for which a value of 1.5° was adopted. Of the three sources modeled, this has the smallest angle of view, so by bracketing this value, given that the flow speeds of all the modeled events are comparable, we are exploring well within the critical cone of the flow, and thus a small range of Doppler factor. The range of Doppler factors never moves the model out of the optically thick domain, and as the peak flux of all models is scaled to the same value, the total flux light curve shows little change with θ . However, while displaying only a slightly higher opacity than 0420-014, in the case of OJ 287 there is little change in the percentage polarization; the percentage polarization of the first component of the modeled flare remains $\sim 7\%$, while that of the second and third components varies between 4 and 6%. The shocks in this model are oblique, with $\eta = 30^\circ$. Depending on the direction of the shock normal, and azimuth of the observer, a change in polar angle can have a similar effect to that in the purely transverse case, can lead to an emission frame angle closer to the plane of compression, or can lead to an angle further from that plane, in which small angular changes have little effect (see Section 3.5). For significantly oblique shocks the

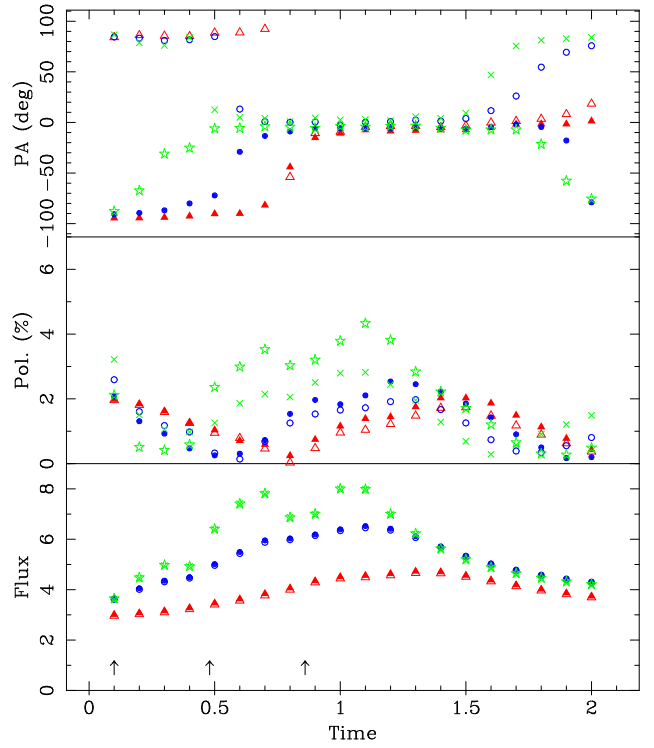


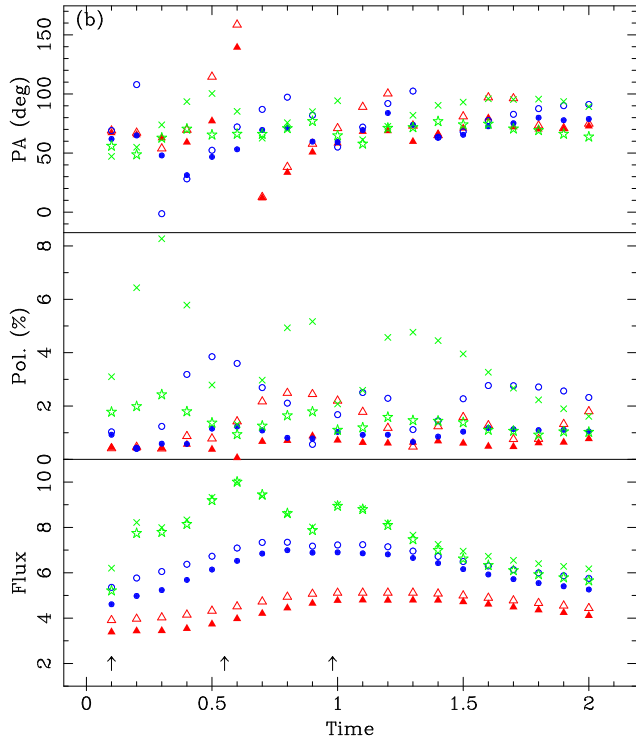
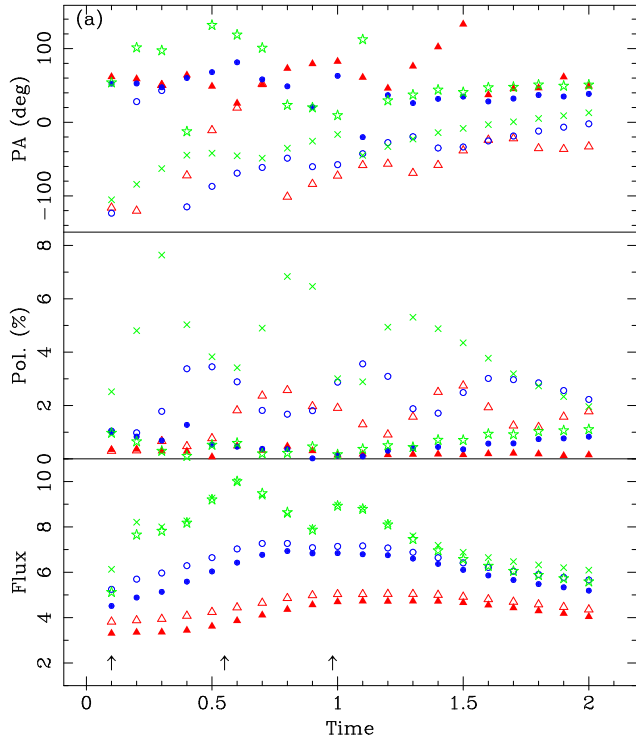
Figure 7. The model for 0420-014 at two values of the azimuthal viewing angle: $\phi = 0$ and 120° . The symbols are as for Figure 1. An mpeg animation showing in detail the variation of the light curves with change in model parameter is available online.

percentage polarization light curves do not provide an unambiguous measure of the viewing angle with respect to the flow axis, and the viewing angle is less well constrained than for transverse shocks.

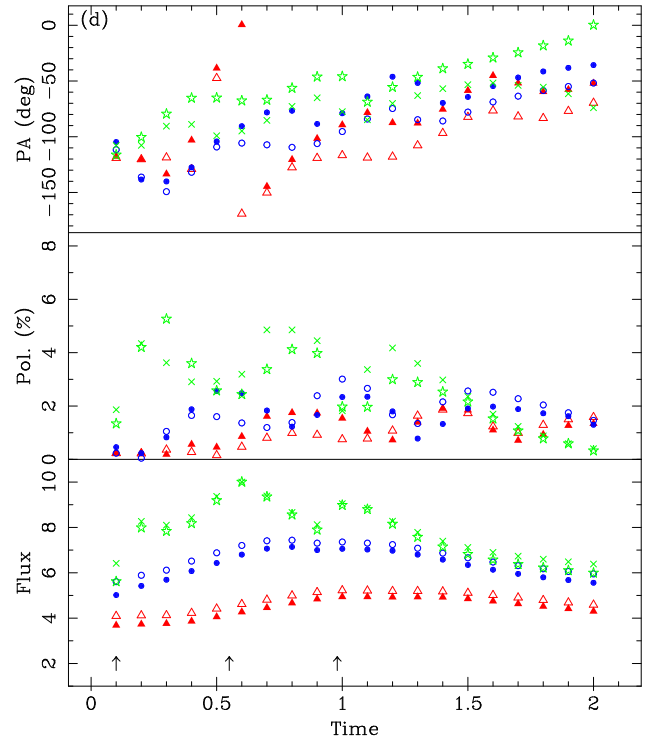
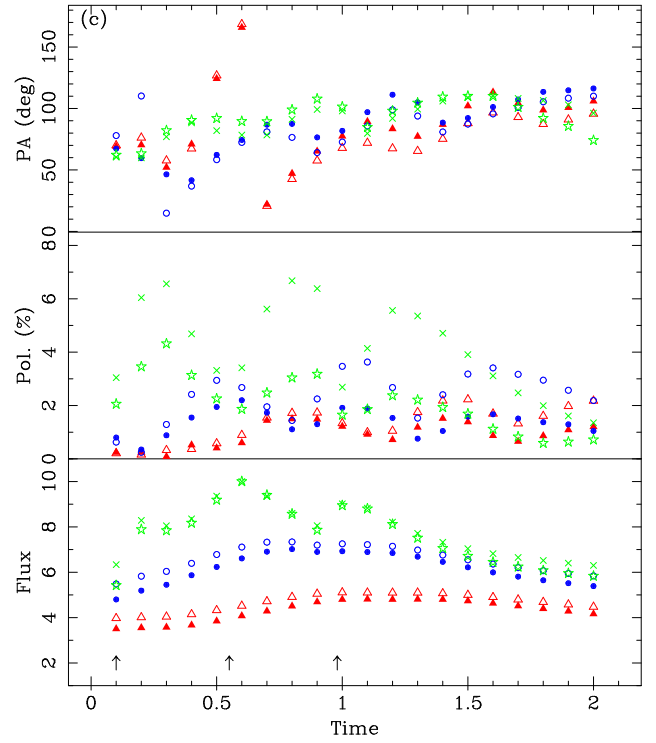
3.5. Azimuthal Viewing Angle

The parameter sequence shown in Figure 7 (animation online) spans the range of ϕ in 30° increments, and is based on the model for 0420-014, for which a value of $\phi = 90^\circ$ was adopted. The figure plots the model for $\phi = 0$ and 120° to show the full range of behavior exhibited. The shock has been offset by 1° from purely transverse, to illustrate how a change of azimuthal viewing angle, which would play no role for purely transverse shocks except for subtle effects associated with particular realizations of the random magnetic field component, changes the model light curves. This therefore quantifies the role of an uncertainty in the shock obliquity. Changes are modest but not negligible, being primarily an increase in the flare percentage polarization by a few percent across the sequence. Recall that the 0420-014 model adopted a polar viewing angle of 4° . The offset from a purely transverse shock structure means that the shocked flow is effectively seen at a polar angle between 3 and 5° , depending upon the observer's azimuth, and indeed the light curves of this sequence are similar to those discussed in Section 3.4, in the range $3.0 \leq \theta \leq 5.0^\circ$. While the modeling well-constrains the polar viewing angle (at least for transverse shocks), the angle is better thought of as the angle to the shock normal, rather than to the flow axis.

The parameter sequences shown in Figure 8 (animations online) span a range of shock obliquities $16^\circ \leq$



$\eta \leq 56^\circ$ for each of the five azimuthal viewing angles $\phi = 0, 45, 90, 135$, and 180° , and is based on the model for OJ 287 for which $\eta = 30^\circ$, $\phi = 45^\circ$, and the shock normal is oriented in azimuthal direction 0° . Given the direction of the shock normal there is symmetry about the azimuthal direction $\phi = 0^\circ$, so we do not display the sequences for $\phi = 225^\circ$ through 315° . There is a well-defined trend with increasing azimuthal angle: at $\phi = 0^\circ$ the peak percentage polarization drops monotonically from ~ 8 to $\sim 0\%$ with increasing shock obliquity,



at $\phi = 45^\circ$ there is a monotonic drop from ~ 8 to $\sim 2\%$, at $\phi = 90^\circ$ there is a rise from 6 to 8%, followed by a drop to 5%, and at $\phi = 135$ and 180° the initial, peak and final polarizations are 5, 7, and 6%, and 3, 6, and 5% respectively.

This variation may be understood as follows. The compression factor determines the increase in density and magnetic field across the shock, and is chosen independently of obliquity. Different obliquities will yield different upstream and downstream flow speeds in the shock

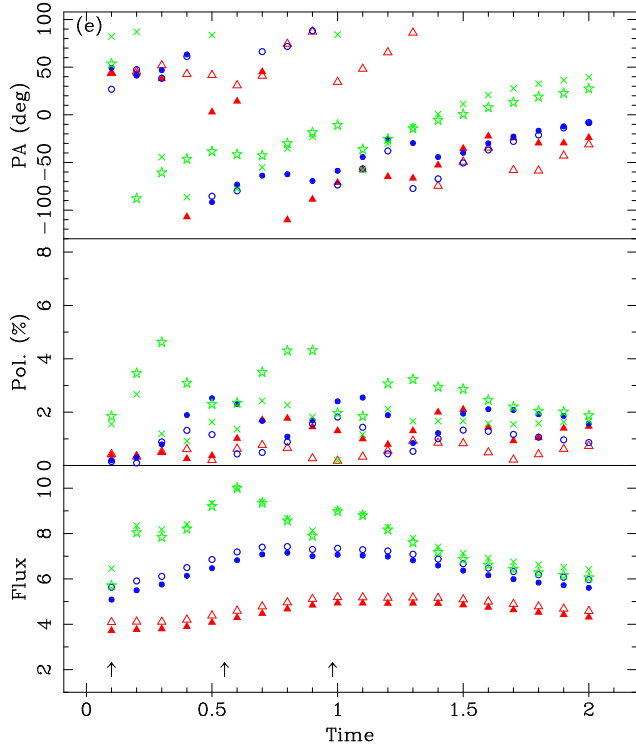


Figure 8. The model for OJ 287 at two extremes of the obliquity: $\eta = 16$ and 56° . Panels (a)-(e) show the cases of $\phi = 0, 45, 90, 135$, and 180° . The symbols are as for Figure 1. mpeg animations showing in detail the variation of the light curves with change in model parameter are available online.

frame, and thus in the observer’s frame; this will lead to different aberrations for the different cases. The compression is normal to the shock plane, the orientation of which (with respect to a given observer) changes with obliquity. For the observer at $\phi = 0$ or 180° the obliquity determines only the orientation between the (pre-aberration) flow frame angle of view and the plane of compression: for $\phi = 0^\circ$, smaller values of the obliquity angle correspond to a flow frame view close to the plane of compression, and increasing the obliquity angle moves the observer farther from that plane, decreasing the percentage polarization; for $\phi = 180^\circ$ and small obliquity angle the flow frame view is quite close to the compression frame, intersects it with increasing obliquity angle, and with a further increase in the obliquity angle passes onto the other side of the plane, leading to an initial rise, and then fall in the percentage polarization. For $\phi = 90^\circ$ and a transverse shock ($\eta = 90^\circ$), the angle between the plane of compression and the (pre-aberration) flow frame angle of view is set solely by the latter, i.e., polar angle and aberration. However, for a maximally oblique shock ($\eta \sim 0^\circ$) the observer will be in the plane of compression for all polar angles of view and aberrations (recall that the shock normal points in the direction $\phi = 0^\circ$). One might thus expect a monotonic decline in percentage polarization with increasing obliquity angle, as that takes the geometry from nearly the maximally oblique case towards the transverse case. However, the change in obliquity angle also leads to a change in the downstream flow speed in both the shock and observer’s frames, and thus to a change in aberration. This initially offsets the anticipated trend, leading to a small initial rise in percentage

polarization.

In summary, the peak percentage polarization spans a narrow range of values as both shock obliquity and observer azimuthal angle are varied (the constraint on obliquity coming largely from the EVPA behavior), except for a limited range of azimuthal angles around $\phi = 0^\circ$ (as noted in Hughes, Aller & Aller 2011), where the value is close to zero. The azimuthal angle is thus not well-constrained. The behavior discussed above further demonstrates that shock obliquity adds uncertainty to the determination of the observer’s polar angle with respect to the flow.

4. 1156+295: THE CASE OF THE ORPHAN FLARE

As noted in Section 3, most interest lies in the complex interaction of multiple events (structure in both VLBI maps and in single-dish light curves suggests that we never see isolated events), so in the above sections we have focused on the consequences of varying individual parameters in the context of representative models for observed radio-band outbursts, rather than single shock events. An additional question that needs to be addressed is the impact of changing the fundamental sub-structure of these composite events: the number of shocks, and their length and compression.

This can be very effectively illustrated by considering the model for 1156+295. The model described in Paper I is based on four shocks of equal length (10% of the quiescent flow), equally separated in start time, and of monotonically decreasing strength – compressions of 0.5, 0.6, 0.7, and 0.8. A number of characteristics of the radio-band outburst with an associated γ -ray flare are well-reproduced by the model, including the total flux density profile and spectrum, the degree and change of percentage polarization, and the swing in the EVPA. But, intriguingly, that radio-band outburst is preceded by one of broadly similar spectral and temporal characteristics in both total and polarized flux, but with no cotemporal γ -ray event.

The ‘orphan flare’ has a total flux light curve similar to those shown for single shock events in Hughes, Aller & Aller (2011), rather than the triangular form of the second event – which, together with sub-structure in the percentage polarization light curve, was the motivating factor behind the choice of a four-shock model. That suggests attempting to model the ‘orphan flare’ with a simpler system of events. Figure 9 shows both the original model from Paper I and a model with two shocks, each 10% of the quiescent flow in length, and starting at dates 2008.40 and 2008.64. Their compressions are 0.6, 0.7 respectively, corresponding to the central pair of shocks used to model the second outburst. The same approach to modeling was used as described in Paper I, which led to a reduced mean field strength (30% as opposed to 50%) and opacity higher by a factor of $\times 2.5$, but in all essential respects the only difference between the models is that of the complexity of the shock system. (A weak ‘precursor’ event has been included to provide an ‘initial state’ of high percentage polarization. This is evident in the polarization data just before the commencement of the flare. There is little evidence from the total flux light curve of significant additional sub-structure, and this precursor could be removed without significantly modifying the model light curves.)

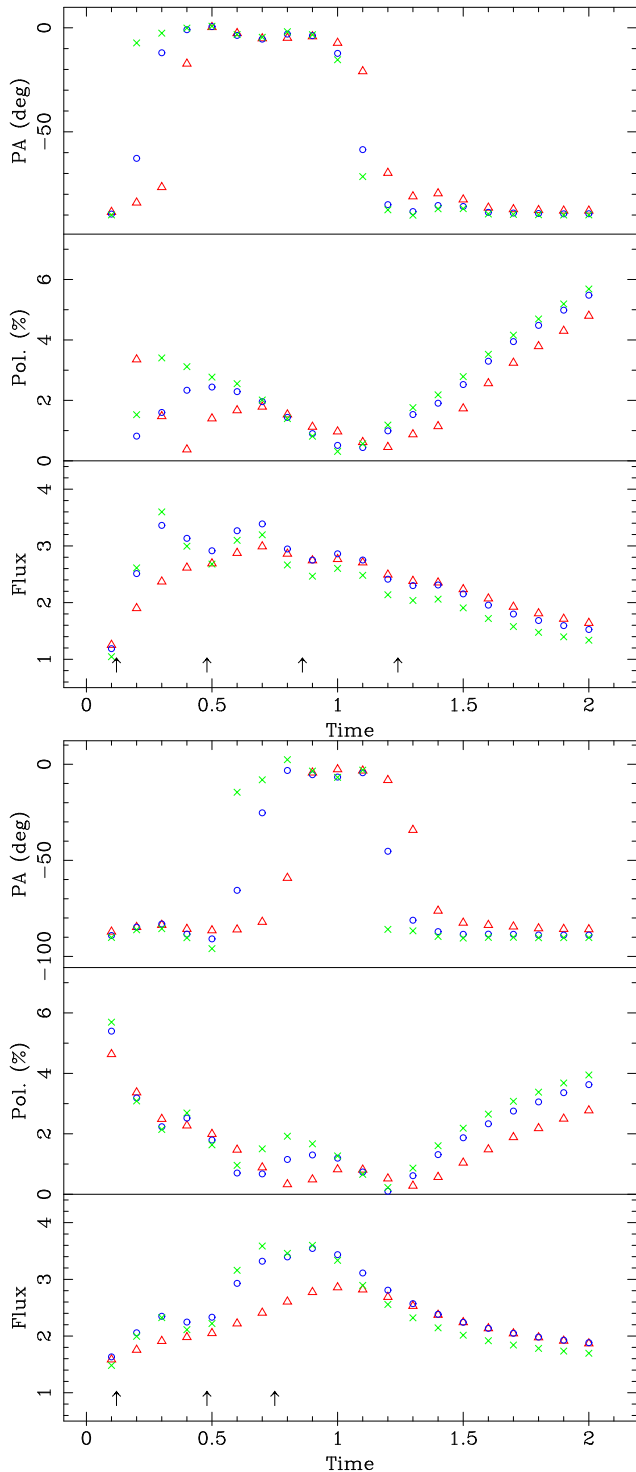


Figure 9. Left panel: The model for 1156+295 from Paper I; this model corresponds to the radio-band outburst accompanied by an event in the γ -ray band. Right: The model for the ‘orphan flare’ exhibited by the same source – in this case there is no corresponding γ -ray event. Symbols are those adopted in Paper I.

It has been suggested by Beloborodov (2000) and Kobayashi & Sari (2001) that γ -ray bursts (GRBs) can be highly efficient if multiple interactions occur between the numerous shells that generate internal shocks. The sub-structure of the γ -ray flare in 1156+295 that peaks around 2010.5 suggests a similar scenario. This leads us to hypothesize that the γ -ray flare originates from GRB-

like interactions upstream of the cm-band outburst region – consistent with these events appearing on the rise portion of the radio band light curve; that these interactions merge some substructures, and order the flow speeds of those that remain, leading to a sequence of a few, noninteracting subcomponents to contribute to the radio-band outburst; and that the absence of a γ -ray flare during the earlier radio-band outburst is due to a simpler flow disturbance with much reduced interaction between components, perhaps because of fewer components as implied by the radio-band model.

Such a scenario does not address why the converse – a γ -ray flare without an associated radio flare – is sometimes seen. The radio-band modeling presented here reveals a significant difference in opacity between sources, and one possible explanation for the absence of a radio counterpart to a γ -ray event is that the event occurs sufficiently far upstream (nearer the base of the flow) that opacity masks the event in the cm-band. By the time the region of accelerated particles and compressed magnetic field has become partially optically thin in the radio-band, radiative and adiabatic losses have reduced the emissivity to a low-enough level that no outburst is evident. A specific variant of this idea has been suggested by MacDonald et al. (2014). In that model, as a plasmoid propagates along a jet spine it passes through a ring of shocked material in the jet sheath. That ring supplies seed photons for inverse-Compton scattering by the plasmoid electrons, leading to a rapidly dissipating γ -ray flare; model light curves agree well with observations of a γ -ray flare seen in the quasar PKS 1510-089. However, much more theoretical work is needed to understand the complex multi-waveband behavior of these sources. Also, it is possible that multiple processes occur, which are not distinguished by current data.

We conclude that modeling as described in this paper has the ability to discriminate between superficially similar radio-band outbursts, revealing fundamental differences between them that have the potential to elucidate important properties of the underlying flows.

5. DISCUSSION

Establishing a well-defined low-energy cutoff to the radiating particle distribution is significant, because a common feature of many mechanisms for producing particles of the appropriate energy involves a ‘heating’ that pushes a subset of low-energy particles into a suprathermal tail of the energy distribution, followed by an ‘acceleration’ that produces a power-law distribution from that tail. [See Eilek & Hughes (1991) for a review of this, but note that multiple phases of acceleration, for example at a sequence of oblique or conical shocks, can result in a flat spectrum with a depleted low energy region, as modeled by Meli & Biermann (2013).] One would therefore expect the distribution to extend down to the reservoir of low-energy particles from which the radiating ones derive. The discussion of Section 3.1 shows that very low values of the cutoff are excluded: in only one case (that of OJ 287) is the cutoff low enough for its effects to be clearly evident in the polarized flux light curves, but, even there, the cutoff is at highly relativistic energy; for the other sources, the absence of evidence for such Faraday effects in the data constrain the cutoff to be even higher. Of course, that means that in those cases the

precise value is ill-constrained, as at these high values, changes in the cutoff value lead to very small changes in the light curves, but that does not invalidate the general conclusion that these flows do not have particle energy spectra extending far below the energy responsible for the cm-band emission. The values found in this analysis are in agreement with the range of values found by Kang et al. (2014) (from 5 to 160, with a median of 55).

The modeling thus provides convincing evidence against the presence of a low-energy particle distribution, either a reservoir of particles on which heating and acceleration act, or resulting from entrainment. It appears that the radiating particles derive not from a low-energy reservoir, but are produced *in situ*, either within the high-energy environment where the jet is first established, or on larger scales: through tapping into a Poynting flux or efficient magnetic field line reconnection (Vincent 2014; Sironi & Spitkovsky 2014). The absence of entrainment is surprising, given the evidence for a random magnetic field, with the implication that the flow is turbulent. However, that a significant fraction of the magnetic field energy is in an ordered component can account for limited transport of particles transverse to the flow axis. These conclusions illustrate a recurrent theme of this discussion, namely that many properties of relativistic jets can be probed effectively only with multifrequency polarization data.

In Section 3.2 we further explored the conclusion of Paper I that, while a turbulent component of the magnetic field is a crucial ingredient of the model for UMR-AO sources, a significant mean (axial) field plays an important role in determining the observed polarization characteristics of the emission. The comparable energy densities of the random and mean components suggest that the latter arises through a non-trivial dynamo process, in which growth of the mean field saturates when the energy densities of the two components are comparable. An alternative possibility is that local instabilities cause a partial dissipation of the bulk flow energy, potentially leading to particle heating/acceleration and turbulent eddies that influence a pre-existing mean field. It might be thought that a considerable degree of fine-tuning would be needed for this to occur without total disruption of the flow, but Porth & Komissarov (2014) have argued that a rapid expansion causes loss of causal connectivity across flows of this type (whether relativistic or not, highly-magnetized or not), allowing the jet spine to exhibit instability, while globally the jet is stable. Indeed, they note that total disintegration of the jet spine does not have to be fatal for the integrity of the larger scale flow. In either scenario – growth from smaller scales, or disruption of pre-existing large-scale field – a significant large-scale field can persist and inhibit the entrainment of thermal matter across the jet boundary. As shown by the sequence of simulations in Figure 2, there is only minor change in the (scaled) total flux light curves as the relative contribution of the mean field is increased; the polarization data are crucial for establishing the fraction of magnetic field energy density in an ordered component, and convincingly fix the value as comparable to, or a little less than, that of the random component.

In addressing the sensitivity of the modeling to the bulk Lorentz factor of the flow (Section 3.3) we are

confronted with the complication of the interplay between several of the model parameters. Broadly, this is a strength of the modeling: for example, the compelling case for our original model of BL Lac (Hughes, Aller & Aller 1989b) came from the fact that the compression able to reproduce the rise in total flux, allowing for Doppler boosting, was that needed to produce an effective order in the magnetic field of the shocked flow which, when observed allowing for the appropriate aberration corresponding to the flow speed and observer’s angle of view to the flow axis, also produced the observed percentage polarization. Despite this complication, the sequence shown in Figure 3 provides a good indication of the sensitivity of the modeling to the choice of the underlying flow speed. By adjusting the ‘opacity parameter’ to preserve the spectral character of the total flux light curve, and maintaining the shock compression across the sequence, the set of light curves highlight the role played by a change in bulk Lorentz factor in determining the percentage polarization – through the change in Lorentz factor of the shocked plasma for fixed observer-frame spectral properties and compression, and thus a change in the flow frame viewing angle for fixed observer angle of view with respect to the flow axis.

It can be argued that an additional parameter change should be ‘folded in’ to this sequence – namely, the viewing angle of the observer with respect to the flow axis – to establish whether recovering the flow frame viewing angle of the original model recovers similar light curves in both total and polarized flux. However, during the iteration process described in Paper I, we have seen that as any parameter is adjusted away from its optimal value, the model light curves deviate from an optimal match to the data in a systematic way that would not be expected to be offset by adjustment in one or more of the other parameters. Taken with the fact that the modeling process leads to a set of observables, such as apparent speed, consistent with contemporaneous VLBI measurements, although we cannot formally prove the uniqueness of the model, the modeling process itself suggests that the model has converged on a unique part of parameter space. In that context, the goal of the current exploration is limited to formally demonstrating the model sensitivity to the parameter under discussion – the bulk Lorentz factor of the flow. Yet again the polarized flux light curve is crucial in limiting viable values of this parameter: for values only a little less than that of the model ($\gamma_f = 5$), or no more than a factor of two higher (corresponding to flows with Lorentz factor < 1.5 on either side of the model value, as measured in the frame of the model flow) the predicted percentage polarization is quite different from that observed. It is encouraging to see how well the modeling is able to narrowly define a set of parameters describing a particular source at some epoch.

From the results presented in Section 3.4 it is clear that, at least for transverse shocks, the observer’s angle of view to the flow axis is the best-constrained of all the parameters – a small change in which leads to very substantial change in the percentage polarization. Being able to define the viewing angle well, independently of VLBI measurements, is a strength of this modeling, as knowledge of that parameter is crucial for the interpretation and modeling of data across the spectrum. In

this context a concern is that the modeling has failed to capture some important flow physics: we have assumed noninteracting, constant velocity shocks in rectilinear motion. At least two of these assumptions are readily shown to be invalid, as extensive VLBI datasets, covering time sequences of a decade or more, such as MOJAVE (Lister et al. 2013; Homan et al. 2014), clearly show curvature, flow acceleration, and, adding yet another layer of complexity, *temporal changes* in properties such as flow curvature. While the spatial and temporal resolution of VLBI data are not sufficient to convincingly address the possibility of shock interactions (and if these are occurring upstream of the 43 GHz core only higher frequency data could probe such dynamics), our result for the orphan and non-orphan flares in the source 1156+295 (Section 4) provides evidence that interactions do occur, and play an important role in establishing the flare properties.

This does not weaken our conclusions, if it is accepted that the modeling is establishing parameters at a particular epoch, for a limited section of a much more extensive flow. While VLBI observations can track components for much longer times than covered by the single dish light curves/models, the most pronounced part of a flare in total and polarized flux, as seen in single-dish light curves, occurs while the disturbance propagates at most tens of jet radii; over this spatial scale global flow curvature will play little role, while secular changes in source structure occur over time scales much longer than that of a single flare. Indeed, the modeling can be used to explore changes in source orientation and flow speed between flare epochs. As discussed in Section 3.5, we can be less confident that the modeling has well-defined the angle between the observer’s line-of-sight and the flow axis if the shocks are oblique. Establishing the range of shock obliquity displayed by sources is itself a useful goal, as it helps to probe the flow dynamics, and the origin of disturbances. However, from the perspective of optimally defining flow properties, to probe the relation between cm-band and γ -ray flares for example, a case can be made for selecting activity due to transverse shocks

(as suggested by 90° swings in EVPA); as noted in Paper I, such cases are quite common, and the selection of sources for modeling is biased towards these cases. Additionally, for interpretation and modeling of the γ -ray data it needs to be established whether there is significant curvature of the flow between cm-band and γ -ray emission regions (the latter upstream of the former – see Paper I), but the modeling provides the observer viewing angle for the former, and thus the ability to deproject curvature seen upstream of this region on VLBI maps, if they exist for a given source/flare. Given the closeness of the observer’s line-of-sight to the flow axis in most cases it seems likely that the actual curvature will prove to be quite small.

Finally, we reiterate the importance of the polarized flux light curves for this modeling. It is quite striking how, looking through the first seven figures of this paper, the opacity, and thus the spectral slope, vary between models for the three sources addressed here, and the overall profile and substructure reflect the number, strength and position of the shocks that contribute to each ‘flare’ – but ultimately all light curves are subtle variants on the van der Laan form (see Section A). It is the richness of the polarized flux behavior that provides the ability to discriminate between parts of parameter space. Existing UMRAO data, and other datasets, whether existing or yet to be acquired, with multi-frequency polarimetry that is well-sampled in the time domain provide a valuable resource for exploring the internal conditions, flow dynamics, and orientation of the γ -ray and cm-band emission regions of AGN jets.

This work was made possible by support from NSF grant NSF-0607523, NASA Fermi grants NNX09AU16G, NNX10AP16G and NNX13AP18G, and by support for the operation of UMRAO from the University of Michigan. Andrew Graus provided valuable assistance with the coding. This research was supported in part through computational resources and services provided by Advanced Research Computing at the University of Michigan, Ann Arbor. We thank an anonymous referee for comments that helped to improve the manuscript.

APPENDIX

RETARDED TIME EFFECTS

The models presented in Hughes, Aller & Aller (2011), Paper I, and the current work, are computed for an instantaneous state of the flow, and do not incorporate retarded time effects. In this appendix it is shown that while the inclusion of such effects does influence the multifrequency total and polarized flux light curves to a discernible degree, the magnitude of the change is not sufficient to warrant using time-intensive retarded time computations in the modeling.

The kinematic models are analytic in the sense that a simple flow geometry and dynamics are established, assuming a conical jet, and flow-filling shocks whose downstream parameters are determined from the jump conditions. However, given the turbulent nature of the flow – a key ingredient of the model – it is necessary to generate realizations of the magnetic field structure using Monte Carlo techniques, for each time step, for each model. Thus, although we do not use hydrodynamic simulations as input to the radiation transfer calculations, the data sets have the complexity of a full hydrodynamic simulation with an evolved, random magnetic field component.

The retarded time needed at a given location for radiation transfer through a particular cell changes with observer orientation, and flow speed (and thus with flow dynamics, including the number, strength, and obliquity of the shocks): thus it changes with a change in almost all model parameters. It follows that inclusion of retarded time effects would impose an enormous computational burden on an extensive exploration of parameter space, because a change in any one parameter would require a recalculation of the retarded state at each location in the flow, at each observer’s time step.

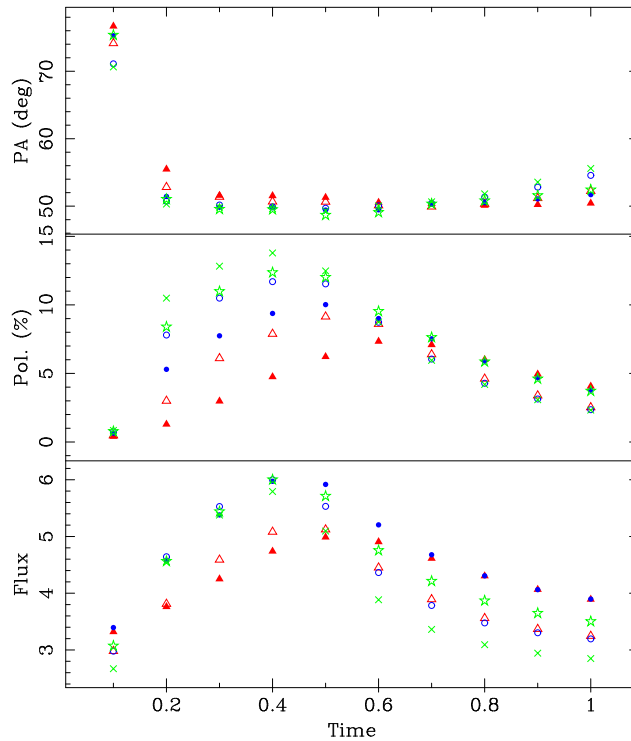


Figure 10. Run A from Hughes, Aller & Aller (2011), which did not include retarded time effects, compared with an identical model which does fully account for such effects, given the 10° viewing angle of the observer. The original model is shown using unfilled triangles, circles and crosses for the frequencies corresponding to the UMRAO frequencies of 4.8, 8.0, and 14.5 GHz (the same convention adopted in Paper I), while the retarded time calculation uses filled triangles, circles, and solid crosses.

Run A of Hughes, Aller & Aller (2011) has been recomputed with retarded time effects included, and the result is shown in Figure 10. The original model is shown using unfilled triangles, circles and crosses for the frequencies corresponding to the UMRAO frequencies of 4.8, 8.0, and 14.5 GHz (the convention adopted in Paper I), while the retarded time calculation uses filled triangles, circles, and solid crosses. Recall (Section 2) that the time coordinate and total flux are subject to an arbitrary scaling: the original and retarded time runs have been scaled independently, as would happen in model-fitting, and do not show the change in burst duration and amplitude that results from the inclusion of retarded time. The character of the variation in total and polarized flux and in the position angle of the polarization vector are largely unchanged, as might be expected given that time delay is “stretching” features significantly only for angles of view close to the jet axis, but that such structures are just those subject to strong projection effects. For both transverse and near-axis views, the propagating structure will be fairly compact, and the total flux variations will have a van der Laan profile (van der Laan 1966); indeed, the light curves for the total flux in propagating shock models since the work of Hughes, Aller & Aller (1989b) all have this character. The percentage polarization is established by the compression and flow-frame viewing angle, independently of retarded time, and fold into the total flux profile to yield a polarized flux light curve similar to that with no retarded time included. In effect, a bounded region of propagating jet plasma always appears ‘blob’-like. The only significant changes are a suppression of the flux at the lowest frequency (with a concomitant reduction in the percentage polarization) due to the longer optical path length, and increased opacity, and a slower fall in flux late in the event, again because of the effective extension of the flow along the line-of-sight.

Quantitatively, the most significant change in total flux occurs near peak outburst but is a reduction by only $\sim 8\%$ at the lowest frequency. A somewhat larger fractional increase is evident late in the outburst, but late-time behavior plays little role in model fitting to data. The concomitant reduction in percentage polarization is only by $\sim 1\%$ at the highest frequency, which is the part of the spectrum most important for model fitting; while the reduction in percentage polarization is by $\sim 3\%$ near peak outburst at the lowest frequency, the percentage polarization at 4.8 GHz for a typical source is low, and also plays only a minor role in the fitting. We conclude that changes in the light curves due to the inclusion of retarded time are too modest to justify the associated computational burden, particularly given that other simplifying assumptions (such as single, noninteracting, constant velocity shocks with rectilinear motion, but see Section 5) are likely to be at least as important in limiting our ability to model radio flares.

REFERENCES

- Ackermann, M., Ajello, M., Allafort, A., et al. 2014, *ApJ*, 786, 157
 Agudo, I., Jorstad, S. G., Marscher, A. P., et al. 2011, *ApJ*, 726, L13
 Aller, M. F., Aller, H. D., & Hughes, P. A. 2003, *ApJ*, 586, 33
 Aller, M. F., Hughes, P. A., Aller, H. D., Latimer, G. E., & Hovatta, T. 2014, *ApJ*, 791, 53 (Paper I)

- Beloborodov, A. M. 2000, *ApJ*, 539, L25
- Blandford, R. D., Königl, A. 1979, *ApJ*, 232, 34
- Cawthorne, T. V., Jorstad, S. G., & Marscher, A. P. 2013, *ApJ*, 772, 14
- Eilek, J. A., & Hughes, P. A. 1991, *Beams and Jets in Astrophysics*, 428
- Homan, D. C., Lister, M. L., Kovalev, Y. Y., et al. 2014, *arXiv:1410.8502*
- Hovatta, T., Lister, M. L., Aller, M. F., et al. 2012, *AJ*, 144, 105
- Hughes, P. A., Aller, H. D., & Aller, M. F. 1985, *ApJ*, 298, 301
- Hughes, P. A., Aller, H. D., & Aller, M. F. 1989a, *ApJ*, 341, 54
- Hughes, P. A., Aller, H. D., & Aller, M. F. 1989b, *ApJ*, 341, 68
- Hughes, P. A., Aller, H. D., & Aller, M. F. 1991, *ApJ*, 374, 57
- Hughes, P. A., Aller, H. D., & Aller, M. F. 2011, *ApJ*, 735, 81
- Jones, T. W., & O'Dell, S. L. 1977, *ApJ*, 214, 522
- Jorstad, S. G., Marscher, A. P., Mattox, J. R., et al. 2001, *ApJ*, 556, 738
- Jorstad, S. G., Marscher, A. P., Smith, P. S., et al. 2013, *ApJ*, 773, 147
- Kang, S., Chen, L., & Wu, Q. 2014, *arXiv:1409.3233*
- Kobayashi, S., & Sari, R. 2001, *ApJ*, 551, 934
- Kovalev, Y. Y., Aller, H. D., Aller, M. F., et al. 2009, *ApJ*, 696, L17
- Lister, M. L., Aller, M. F., Aller, H. D., et al. 2013, *AJ*, 146, 120
- MacDonald, N. R., Marscher, A. P., Jorstad, S. G., & Joshi, M. 2014, *American Astronomical Society Meeting Abstracts #224*, 224, #410.02
- Marscher, A. P. 2006, *Relativistic Jets: The Common Physics of AGN, Microquasars, and Gamma-Ray Bursts*, 856, 1
- Max-Moerbeck, W., Hovatta, T., Richards, J. L., et al. 2014, *MNRAS*, 445, 428
- Meli, A., & Biermann, P. L. 2013, *A&A*, 556, A88
- Park, K., Blackman, E. G., & Subramanian, K. 2013, *Phys. Rev. E*, 87, 053110
- Porth, O., & Komissarov, S. S. 2014, *arXiv:1408.3318*
- O'Sullivan, S. P., McClure-Griffiths, N. M., Feain, I. J., Gaensler, B. M., & Sault, R. J. 2013, *MNRAS*, 435, 311
- Rogachevskii, I., & Kleorin, N. 2003, *Phys. Rev. E*, 68, 036301
- Sironi, L., & Spitkovsky, A. 2014, *ApJ*, 783, L21
- Valtaoja, E., & Teräsranta, H. 1995, *A&A*, 297, L13
- Valtaoja, E., & Teräsranta, H. 1996, *Ap&SS*, 120, 491
- van der Laan, H. 1966, *Nature*, 211, 1131
- Vincent, S. 2014, *International Journal of Modern Physics Conference Series*, 28, 60189
- Yousef, T. A., Heinemann, T., Schekochihin, A. A., et al. 2008, *Physical Review Letters*, 100, 184501
- Zrake, J. 2014, *arXiv:1407.5626*